CHAPTER-3

MODELLING AND EXERGY ANALYSIS OF SINGLE EFFECT H_2O–LiCl ABSORPTION REFRIGERATION SYSTEM

CHAPTER-3

MODELLING AND EXERGY ANALYSIS OF SINGLE EFFECT H_2O–LiCl ABSORPTION REFRIGERATION SYSTEM

3.1 Introduction

As discussed in Chapter 2, lot of researches have been done to evaluate performance of half, single, double and triple effect vapour absorption refrigeration system (VARS) configurations with various working solution pairs. In some studies, the performance of the VARS configurations were analyzed on the basis of first law (energy analysis) while in some other studies, the analyses were done on the basis of second law of thermodynamics (exergy analysis). Some studies, available in the literature, also discuss about properties of various binary, ternary and quaternary mixtures as working solution pairs for application in VARS.

It was pointed out in Chapter 2 that H_2O–LiCl binary mixture also has the potential to be used as working fluid in VARS. In some research works [1–4], VARS performance was evaluated with H_2O–LiCl as solution pair; however these were totally based on energy analysis. Energy analysis has certain limitations which were highlighted earlier in Chapter 1 and 2 and these limitations of energy analysis can be overcome by carrying out both the energy and exergy analyses together for complete depiction of system performance characteristics. Unfortunately, exergy analysis of single effect H_2O–LiCl VARS was not found in the literature. The exergetic performance of single effect H_2O–LiCl VARS was not evaluated in any of the previous research studies. Contrary to this, there are plenty of research articles available in the literature which is related to energy and exergy analysis of VARSs operated with H_2O–LiBr and NH_3–H_2O, the two most common solution pairs. In this chapter, detail energy and exergy based parametric analysis of a single effect H_2O–LiCl VARS is presented. Exergetic efficiency and component irreversibility of the H_2O–LiCl VARS are evaluated with the help of a MATLAB code and presented along with the energy based performance. A performance comparison of the single effect H_2O–LiCl VARS is also provided with the H_2O–LiBr based system under identical conditions.

Crystallization of salt solution is a major problem with salt based absorbent in VARS. The crystallization characteristics of H_2O–LiCl solution are different from H_2O–

LiBr and other salt based binary mixtures. In any situation, the maximum salt concentration in the solution should not exceed the crystallization limit to avoid blockage of the flow passages and maintain continuous system operation. This is entirely dependent on the system operating temperatures. Particularly with H_2O–LiCl, the risk to crystallization is high because the maximum solution concentration for the H_2O–LiCl system is 50% as compared to 65% with H_2O–LiBr. In articles [5–7], the formulations for thermodynamic properties of H_2O–LiCl solutions were provided for the composition range from pure water to 50% wt. Grover et al. [1] also took the upper limit of solution concentration as 51% and accordingly the operating temperatures were selected. If the VARS components temperatures are not selected carefully, then it might lead to a situation where maximum solution concentration may exceed 50% leading to crystallization of the salt solution. This constitutes an inverse problem, and therefore, to estimate the generator, condenser, evaporator and absorber temperatures of the single effect VARS, a differential evolution (DE) based inverse method is used, considering the weak solution concentration (X_{ws}) below 50% as objective function at Generator exit. Details about DE are available in the articles [8–11], hence these are not repeated in this thesis.

3.2 Description of single effect LiCl−H_2O VARS

The single effect H_2O–LiCl based VARS schematic is shown in Fig. 3.1. It consists of the basic components viz. the generator, condenser, evaporator, absorber, solution pump (SP) and two expansion valves (ExV1 and ExV2). A solution heat exchanger (SHE) is considered between the generator and absorber to preheat the absorber leaving strong H_2O–LiCl solution with the heat of high temperature weak solution that flows back from the generator to the absorber.

3.3 Assumptions

It is assumed that the system operates under steady state. The refrigerant (water) at condenser exit is saturated liquid and it is saturated vapor at the evaporator exit. Pressure losses in the pipelines and heat exchangers are neglected. Heat loss between the system and surroundings is negligible. The generator heat source is saturated steam with its saturation temperature 10°C higher than the generator temperature (T_G). The reference system is water at 25°C and 1.01325 bar. In exergy analysis, kinetic and potential energy

effects are neglected. Further, it is assumed that the condenser and absorber are water cooled and the refrigerant in the evaporator derives the latent heat of evaporation from water to produce chilled water for cooling. The evaporator cooling load ($\dot{Q}_E$) is taken as 350 kW, although it is possible to investigate the effect of cooling load variation on various performance parameters. Usually with cooling load, the mass flow rates and thermal loads in various VARS components increase proportionately. COP and exergy efficiency remain the same however the irreversibility in various components increases with increase in cooling load. As the results corresponding to cooling load variation is known from previous studies [11, 12], hence, the cooling load variation is avoided in this work and instead a fixed cooling load is considered. In Ref. [13], the author considered a cooling load of 300 kW, therefore a cooling load of this range but slightly higher is considered in this Chapter. In fact, the assumptions which are made here for steady state analysis of the single effect VARS are more or less similar to the assumptions made in Refs. [11–13]. Other assumed system parameters are shown in Table 3.1.

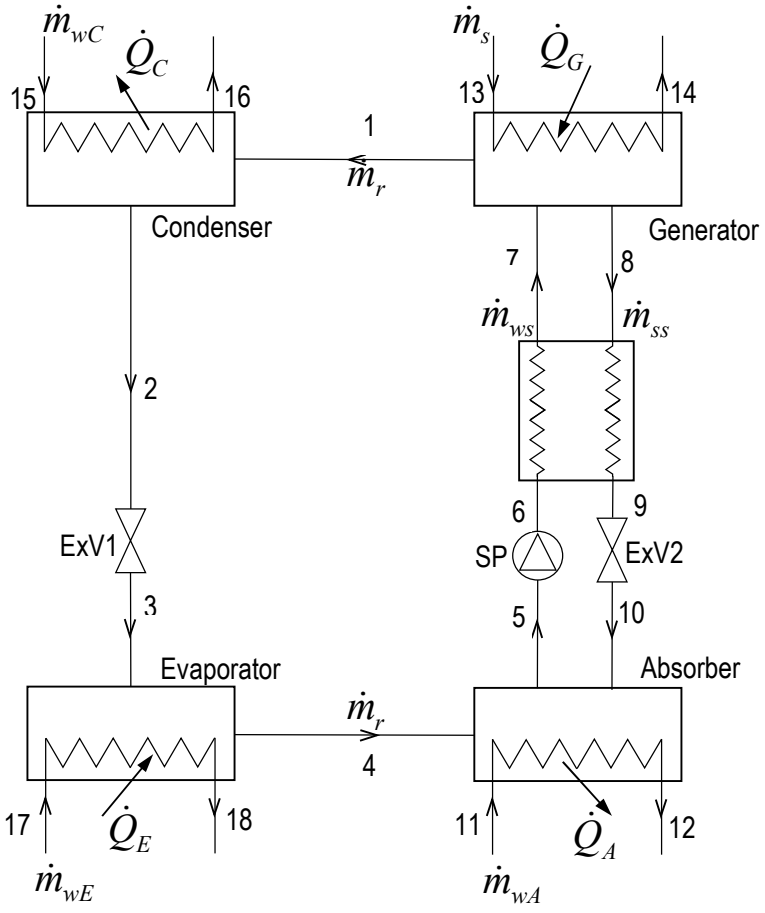

Fig.3.1: Schematic of the single effect H_2O–LiCl VARS

Table 3.1: Assumed Parameter

Parameter	Value
Effectiveness of SHE	0.75
Water temperature at absorber inlet (ºC)	T_A–8
Water temperature at absorber outlet (ºC)	T_A–3
Water temperature at condenser inlet (ºC)	T_C–7
Water temperature at condenser outlet (ºC)	T_C–2
Water temperature at evaporator inlet (ºC)	T_E+7
Water temperature at evaporator outlet (ºC)	T_E+2

3.4 Thermodynamic formulations

The refrigerant (water) mass flow rate is calculated from known evaporator cooling load as follows.

$$\dot{m}_r = \frac{\dot{Q}_E}{h_4 - h_3} \tag{3.1}$$

Weak and strong solution concentrations $(X_{ws}$ and $X_{ss})$ are considered to be temperature dependent and these are calculated using correlation of Grover et al. [1]. The mass flow rates of strong and weak solution are calculated using equations taken from the Ref. [14]**.** Thermodynamic properties of water at liquid and vapour state are computed from International Associations for the Properties of Water and Steam (IAPWS) formulation 1997 [15]**.** Thermodynamic properties of H_2O–LiCl solution are calculated using the correlations of Patek and Klomfar [7]. Heat load in the generator $(\dot{Q}_G)$, absorber $(\dot{Q}_A)$ and condenser $(\dot{Q}_C)$ can be calculated from known values of enthalpy and mass flow rate at the relevant states. The amount of saturated steam required for the VARS generator is calculated from the following equation.

$$\dot{m}_s = \frac{\dot{Q}_G}{h_{s,G_{in}} - h_{w,G_{out}}} \tag{3.2}$$

Cooling water flow rates through the evaporator, absorber and condenser are determined from heat balance applied to these devices. The COP and exergetic efficiency of the VARS are defined as follows:

$$COP = \frac{\dot{Q}_E}{\dot{Q}_G + \dot{W}_p}, \ \dot{W}_p \text{ is the solution pump work} \tag{3.3}$$

$$\text{VARS exergy efficiency, } \eta = \frac{\left(\dot{E}x_{w,E_{out}} - \dot{E}x_{w,E_{in}}\right)}{\left(\dot{E}x_{s,G_{in}} - \dot{E}x_{w,G_{out}}\right) + \dot{W}_{SP}} \tag{3.4}$$

Carnot based coefficient of performance (COP) is

$$(COP)_C = \left(\frac{T_G - T_A}{T_G}\right)\left(\frac{T_E}{T_C - T_E}\right) \tag{3.5}$$

Effectiveness method is used to calculate weak and strong solution temperatures of SHE outlet. Exergy destruction (irreversibility) in the generator, condenser, evaporator, absorber and SHE are calculated using the following equations.

$$\dot{I}_G = \dot{m}_{ss}\psi_7 - \dot{m}_{ws}\psi_8 - \dot{m}_r\psi_1 + \dot{m}_s\left(\psi_{13} - \psi_{14}\right) \tag{3.6}$$

$$\dot{I}_C = \dot{m}_r(\psi_1 - \psi_2) + \dot{m}_{w,C}\left(\psi_{15} - \psi_{16}\right) \tag{3.7}$$

$$\dot{I}_E = \dot{m}_r(\psi_3 - \psi_4) + \dot{m}_{w,E}\left(\psi_{17} - \psi_{18}\right) \tag{3.8}$$

$$\dot{I}_A = \dot{m}_r\psi_4 + \dot{m}_{ws}\psi_{10} - \dot{m}_{ss}\psi_5 + \dot{m}_{w,A}\left(\psi_{11} - \psi_{12}\right) \tag{3.9}$$

$$\dot{I}_{SHE} = \dot{m}_{ws}(\psi_8 - \psi_9) - \dot{m}_{ss}(\psi_7 - \psi_6) \tag{3.10}$$

In the above equations, $\psi = (h - h_0) - T_0(s - s_0)$ is the specific exergy of the flow streams, $\dot{m}_{w,C}$, $\dot{m}_{w,E}$ and $\dot{m}_{w,A}$ are the water flow rates through the condenser, evaporator and the absorber respectively. To evaluate ψ, enthalpy (h) and entropy (s) at various state points are calculated [7, 15]. The enthalpy and entropy at the reference state (h_0, s_0) are calculated assuming reference system of water at pressure 1.01325 bar and temperature 25°C. Irreversibility in the two expansion valves ($\dot{I}_{ExV1}$ and $\dot{I}_{ExV2}$) and the solution pump $(\dot{I}_{SP})$ are calculated using equations (3.11), (3.12) and (3.13) respectively.

$$\dot{I}_{ExV1} = \dot{m}_r(\psi_2 - \psi_3) \tag{3.11}$$

$$\dot{I}_{ExV2} = \dot{m}_{ws}(\psi_9 - \psi_{10}) \tag{3.12}$$

$$\dot{I}_{SP} = \dot{m}_{ss}(\psi_6 - \psi_5) \tag{3.13}$$

Total irreversibility $(\dot{I}_{tot})$ is the sum of irreversibility in all the components. In calculation of exergy at various states, the chemical exergy is however not considered. The chemical exergy may particularly arise in case of the salt solution. Ignoring chemical exergy would not affect the irreversibility calculation of the VARS components due to negligible departure of chemical substances from the cycle to the environment [13]. Chemical exergy would remain same at inlet and outlet of a given VARS component and hence, would get cancelled out in the irreversibility calculation.

3.5 Results and discussion

3.5.1 Estimation of operating temperatures

The temperature combinations estimated from the DE based inverse method are shown in Table 3.2. In every test run, different combinations of component temperatures are obtained and all these combinations fulfill the set objective function i.e. $X_{ws} \leq 50\%$. $X_{ws} \leq 50\%$ (Say e.g. $X_{ws} = 49\%$ in some of the estimations) is considered because this is the limiting value up to which the thermodynamic property equations used in this Chapter are valid.

The searching ranges of temperatures specified for estimation of component temperatures (T_E, T_G, T_C and T_A) are as given below.

Range [T_E: 1–10°C; T_G: 50–90°C; T_C: 20–50°C; T_A: 30–40°C]

Some arbitrary values of the component temperatures are randomly chosen from the range of specified values during each generation in the DE based search algorithm. The optimization process continues and is terminated within 50 generations (specified) during which the objective function $f = \left(X_{ws} - \widetilde{X}_{ws}\right)^2$ also attains a very small value of the order of zero. $\widetilde{X}_{ws}$ is the weak solution concentration corresponding to the

temperatures (T_E, T_G, T_C and T_A) obtained in the next generation during the optimization process. Many such combinations can be estimated, however in Table 3.2, only 34 combinations are shown with evaporator temperature ranging from 2°C to 9°C. The minimum T_G shown in Table 3.2 is 63°C while the maximum T_G is 84°C. Similarly the minimum estimated T_C is 25°C and maximum 45°C is obtained. The minimum and maximum T_A are 30°C and 38°C respectively. Thus, it is seen that all these estimated temperature values fall within the prescribed range of lower and upper bound of the component temperatures. The system now can be operated at any of these combinational temperatures with X_{ws} always within 50% limit. From the estimated temperature combinations, it is seen that T_G and T_C are directly linked with one another. When a lower T_G is estimated by the inverse method, the corresponding estimated T_C also reduces proportionately and vice versa. This is because X_{ws} is T_G and T_C dependent as per the correlation of Grover et al. [1].

Table 3.2: Estimated combinations of operating temperatures with X_{ws} ≤50% as objective function

Test Run	Temperature (ºC)			
	T_E	T_G	T_C	T_A
1	2	70	31	38
2	2	78	39	35
3	3	73	34	35
4	3	71	33	37
5	3	79	41	33
6	3	72	34	33
7	3	72	34	35
8	4	76	37	32
9	4	70	31	31
10	4	73	34	31
11	4	69	31	35
12	4	74	36	30
13	5	71	32	36
14	5	72	33	35
15	5	66	28	35
16	5	68	30	37
17	5	75	37	34
18	6	72	33	37
19	6	75	36	33
20	6	79	41	31
21	6	72	34	34
22	6	75	37	34
23	7	74	35	36
24	7	80	41	36
25	7	77	39	36
26	7	84	45	36
27	8	73	34	34
28	8	79	40	34
29	8	63	25	37
30	8	74	36	37
31	8	70	32	37
32	9	79	40	37
33	9	82	44	33
34	9	66	28	34

3.5.2 H_2O–LiCl VARS performance at estimated temperatures

The energetic and exergetic performance of the H_2O–LiCl VARS has been simulated with the MATLAB program developed using the estimated combinations of temperatures. The results concerning weak and strong solution concentrations, components' thermal loads and mass flow rates with respect to the above combinational temperatures are shown in Table 3.3 (a–b). It is seen that X_{ws} is less than 50% for all these combinations while X_{ss} varies. The heat loads in the VARS components ($\dot{Q}_G$, $\dot{Q}_C$ and $\dot{Q}_A$) change with the component temperatures being different at various test runs. Mass flow rates of steam ($\dot{m}_s$), refrigerant ($\dot{m}_r$), weak solution ($\dot{m}_{ws}$) and strong solution ($\dot{m}_{ss}$) also vary accordingly. The irreversibility occurring in various system components, total system irreversibility, COPs (actual and Carnot), VARS exergy efficiency and solution pump (SP) power are presented in Table 3.4 (a–b). Highest actual and Carnot COP (0.877 and 1.401 respectively) are obtained in the 34th combination at T_E =9°C, T_G =66°C, T_C =28°C and T_A =34°C although the corresponding exergy efficiency (24.104%) and system irreversibility (41.66 kW) are not the maximum and minimum at this combination. The maximum exergy efficiency (34.584%) and minimum total system irreversibility (31.914 kW) are obtained with T_E =2°C, T_G =70°C, T_C =31°C and T_A =38°C in the 1st combination. The corresponding actual and Carnot COP with estimated temperatures of the 1st combination are 0.814 and 0.885 respectively. Further it is seen that the system COP improves at relatively higher T_E and lower values of T_G, T_C and T_A. However from the results in Tables 3.3 (a–b) and 3.4 (a–b), it is difficult to show the variation of heat loads, mass flow rates and the other performance parameters (exergy efficiency and irreversibility) with changing component temperatures. Therefore the MATLAB program which was developed earlier for simulating VARS performance was later modified to consider variation of the component temperatures. Results are obtained by varying the evaporator temperature at two different condenser and absorber temperatures while keeping X_{ws} within 50% limit. Generator temperature is also varied to show performance variation with T_G at two different condenser and absorber temperatures.

Table 3.3a: Performance data with respect to the temperature combinations estimated during test runs 1 to 17 in Table 3.2

Combinations	X_{ws}	X_{ss}	Heat Load (kW)			Mass Flow Rate (kg/s)			
			$\dot{Q}_G$	$\dot{Q}_A$	$\dot{Q}_C$	$\dot{m}_s$	$\dot{m}_r$	$\dot{m}_{ws}$	$\dot{m}_{ss}$
1	0.498	0.438	430.042	410.530	368.681	0.186	0.147	1.073	1.220
2	0.499	0.408	432.839	410.876	371.147	0.189	0.150	0.668	0.818
3	0.499	0.400	422.610	402.722	369.311	0.184	0.148	0.596	0.744
4	0.490	0.420	426.856	407.355	368.726	0.185	0.148	0.890	1.038
5	0.490	0.380	427.906	406.019	371.196	0.187	0.150	0.517	0.667
6	0.490	0.380	418.428	398.872	369.031	0.182	0.148	0.510	0.658
7	0.490	0.400	422.753	403.081	369.031	0.184	0.148	0.658	0.806
8	0.499	0.362	418.400	398.016	369.947	0.183	0.149	0.390	0.539
9	0.498	0.351	409.438	391.005	368.112	0.177	0.147	0.352	0.499
10	0.499	0.351	413.095	393.710	369.025	0.180	0.148	0.352	0.500
11	0.489	0.392	415.691	397.370	367.833	0.180	0.147	0.591	0.739
12	0.490	0.341	413.468	393.721	369.357	0.180	0.149	0.341	0.490
13	0.499	0.393	416.478	397.903	368.131	0.181	0.147	0.551	0.698
14	0.499	0.383	416.000	397.140	368.434	0.181	0.148	0.490	0.638
15	0.488	0.383	409.116	392.097	366.649	0.177	0.146	0.537	0.684
16	0.489	0.403	415.680	397.940	367.249	0.180	0.147	0.695	0.842
17	0.490	0.373	419.133	399.252	369.377	0.183	0.149	0.476	0.624

Table 3.3b: Performance data with respect to the temperature combinations estimated during test runs 18 to 34 in Table 3.2

Combinations	X_{ws}	X_{ss}	Heat Load (kW)			Mass Flow Rate (kg/s)			
			$\dot{Q}_G$	$\dot{Q}_A$	$\dot{Q}_C$	$\dot{m}_s$	$\dot{m}_r$	$\dot{m}_{ws}$	$\dot{m}_{ss}$
18	0.499	0.395	417.087	398.491	368.150	0.181	0.148	0.562	0.710
19	0.499	0.355	414.221	394.793	369.064	0.181	0.148	0.366	0.514
20	0.490	0.335	416.750	396.023	370.323	0.182	0.150	0.325	0.474
21	0.490	0.365	412.801	394.233	368.174	0.179	0.148	0.433	0.581
22	0.490	0.365	416.638	397.103	369.089	0.182	0.149	0.435	0.583
23	0.499	0.377	415.457	396.590	368.473	0.181	0.148	0.456	0.604
24	0.499	0.377	423.291	402.467	370.317	0.185	0.149	0.462	0.612
25	0.490	0.377	420.400	400.473	369.416	0.184	0.149	0.497	0.646
26	0.498	0.377	428.663	406.502	371.566	0.189	0.151	0.470	0.621
27	0.499	0.349	408.948	390.776	367.885	0.178	0.148	0.343	0.490
28	0.499	0.349	416.253	396.169	369.719	0.182	0.149	0.347	0.496
29	0.486	0.379	401.397	386.228	364.922	0.173	0.145	0.512	0.657
30	0.490	0.379	415.690	397.046	368.212	0.181	0.148	0.504	0.652
31	0.489	0.379	410.444	393.082	367.003	0.178	0.147	0.504	0.651
32	0.499	0.371	418.765	398.919	369.431	0.183	0.149	0.430	0.578
33	0.489	0.331	416.876	396.115	370.384	0.183	0.150	0.314	0.464
34	0.488	0.341	399.066	383.324	365.530	0.172	0.146	0.338	0.484

Table 3.4a: Irreversibility and other performance data with respect to estimated temperature combinations (1 to 17) in Table 3.2

Combinations	Irreversibility (kW)							*COP*	$(COP)_c$	η (%)	SP Power (Watt)
	$\dot{I}_G$	$\dot{I}_C$	$\dot{I}_E$	$\dot{I}_A$	$\dot{I}_{SHE}$	$\dot{I}_{ExV1}$	$\dot{I}_{tot}$				
1	16.880	6.065	6.093	0.132	1.787	0.956	31.914	0.814	0.885	34.584	2.411
2	17.924	5.803	6.093	1.265	2.158	1.550	34.793	0.809	0.911	30.677	2.599
3	19.119	5.960	6.050	1.763	1.554	1.084	35.530	0.828	0.978	31.724	1.702
4	17.439	5.959	6.050	0.510	1.741	1.016	32.714	0.820	0.909	32.347	2.271
5	19.363	5.703	6.050	1.873	2.034	1.624	36.645	0.818	0.949	28.872	2.301
6	20.265	5.926	6.050	1.743	1.472	1.084	36.538	0.837	1.007	32.511	1.476
7	18.738	5.926	6.050	1.145	1.613	1.084	34.556	0.828	0.955	32.179	1.843
8	21.627	5.858	6.007	3.299	1.491	1.220	39.500	0.837	1.058	28.866	1.422
9	23.368	6.056	6.007	3.425	1.100	0.819	40.775	0.855	1.167	32.169	0.878
10	22.879	5.955	6.007	3.517	1.267	1.010	40.634	0.847	1.121	30.492	1.078
11	19.750	6.021	6.007	1.644	1.260	0.819	35.500	0.842	1.020	32.181	1.352
12	22.942	5.856	6.007	3.270	1.369	1.148	40.590	0.847	1.098	30.032	1.189
13	19.778	6.017	5.964	2.592	1.239	0.814	36.404	0.840	1.048	29.158	1.351
14	20.399	5.984	5.964	2.921	1.262	0.875	37.403	0.841	1.065	28.760	1.309
15	20.840	6.120	5.964	2.107	0.977	0.592	36.600	0.856	1.105	32.133	0.981
16	18.961	6.051	5.964	1.589	1.188	0.699	34.452	0.842	1.011	30.606	1.429
17	20.183	5.819	5.964	2.711	1.520	1.141	37.338	0.835	1.024	27.347	1.649

Table 3.4b: Irreversibility and other performance data with respect to estimated temperature combinations (18 to 34) in Table 3.2

Combinations	Irreversibility (kW)							*COP*	$(COP)_c$	η (%)	SP Power (Watt)
	$\dot{I}_G$	$\dot{I}_C$	$\dot{I}_E$	$\dot{I}_A$	$\dot{I}_{SHE}$	$\dot{I}_{ExV1}$	$\dot{I}_{tot}$				
18	19.415	5.979	5.921	2.909	1.251	0.809	36.286	0.839	1.048	26.741	1.452
19	22.124	5.881	5.921	4.142	1.289	0.998	40.355	0.845	1.123	25.796	1.236
20	22.630	5.690	5.921	4.214	1.543	1.355	41.352	0.840	1.087	24.305	1.529
21	21.184	5.912	5.921	3.215	1.221	0.870	38.323	0.848	1.098	27.019	1.235
22	20.750	5.815	5.921	3.288	1.415	1.065	38.253	0.840	1.061	25.646	1.510
23	20.460	5.909	5.880	3.826	1.246	0.865	38.186	0.842	1.095	24.199	1.370
24	19.672	5.718	5.880	3.927	1.665	1.272	38.133	0.827	1.027	21.920	2.035
25	19.504	5.747	5.880	3.310	1.555	1.127	37.123	0.833	1.025	22.948	1.899
26	19.256	5.598	5.880	3.936	1.992	1.586	38.248	0.817	0.991	20.615	2.615
27	22.799	5.937	5.838	4.916	1.057	0.742	41.289	0.856	1.218	23.011	0.995
28	21.950	5.745	5.838	5.029	1.399	1.121	41.082	0.841	1.123	20.833	1.492
29	21.605	6.212	5.838	3.070	0.663	0.319	37.707	0.872	1.279	27.532	0.677
30	19.699	5.838	5.838	3.519	1.285	0.860	37.038	0.842	1.070	22.316	1.561
31	20.310	5.969	5.838	3.397	1.032	0.633	37.179	0.853	1.127	23.974	1.178
32	20.155	5.740	5.797	4.729	1.428	1.046	38.895	0.836	1.086	18.985	1.758
33	22.412	5.586	5.797	5.319	1.544	1.331	41.989	0.840	1.112	18.368	1.733
34	23.981	6.101	5.797	4.662	0.724	0.395	41.660	0.877	1.401	24.104	0.604

3.5.3 Performance variation with T_E at two different condenser and absorber temperatures

Fig. 3.2 shows the variation of COP and exergy efficiency with evaporator temperature at condenser temperatures of 36°C and 40°C. During this variation, T_G and T_A are kept fixed at 75°C and 35°C respectively. With T_G fixed at 75°C, the condenser temperature cannot be lowered below 36°C because X_{ws} in that case becomes higher than 50% and the equations used for calculating H_2O–LiCl solution properties in this simulation are valid only for $X_{ws} < 50\%$. When T_E is varied from 2 to 8°C, at T_C=36°C, X_{ws} remains fixed at 49.92% while X_{ss} decreases from 40.79% at T_E=2°C to 35.89% at T_E=8°C. It is seen that COP increases with increase in T_E and also it is more at lower condenser temperature. With increase in T_E, the heat loads in the VARS components decrease particularly in the generator and the absorber (shown in Table 3.5). Similarly the mass flow rates ($\dot{m}_{ws}$, $\dot{m}_{ss}$ and $\dot{m}_s$) also show a decreasing trend with increasing T_E. This is the reason that COP increases with increase in T_E due to reduction mainly in the generator heat load. Refrigerant mass flow rate ($\dot{m}_r$) also reduces slightly with T_E. Similar variation of COP with T_E was also reported by Grover et al. [1]. Further, when T_C is increased from 36°C to 40°C, the VARS components' heat loads and the mass flow rates increase and COP therefore becomes less at higher T_C. Exergy efficiency on the other hand shows an opposite trend (decreases with increasing evaporator temperature); their values at T_C=36°C and T_C=40°C at various evaporator temperatures do not differ much. Lower exergy efficiency at higher T_E was also observed by Gomri [13] in the comparative study of single and double effect H_2O–LiBr VARS. Exergy efficiency reduces with T_E mainly due to reduction in decrease of evaporator water exergy at higher T_E which is more prominent than the decrease in steam exergy at the generator side and the SP power (Equation 3.4). Decrease in generator steam exergy and SP power slightly reduce with T_E due to reduction in $\dot{m}_s$ (because $\dot{Q}_G$ reduces) and $\dot{m}_{ws}$. Again the exergy efficiency at T_C=36°C is more than its value at T_C=40°C, however when the evaporator temperature is increased, the difference between exergy efficiency values at the two condenser temperatures decreases.

Table 3.5: Variation of component heat loads and mass flow rates with T_E at two different condenser temperatures

T_E (°C)	At T_G=75°C, T_A=35 and T_C=36°C						At T_G=75°C, T_A=35 and T_C=40°C					
	Heat Load (kW)			Mass Flow Rate (kg/s)			Heat Load (kW)			Mass Flow Rate (kg/s)		
	$\dot{Q}_G$	$\dot{Q}_C$	$\dot{Q}_A$	$\dot{m}_{ws}$	$\dot{m}_{ss}$	$\dot{m}_s$	$\dot{Q}_G$	$\dot{Q}_C$	$\dot{Q}_A$	$\dot{m}_{ws}$	$\dot{m}_{ss}$	$\dot{m}_s$
2	428.44	370.21	407.51	0.664	0.813	0.187	440.43	370.32	418.71	1.119	1.269	0.192
3	425.39	369.93	404.84	0.597	0.746	0.185	434.74	370.03	413.55	0.953	1.103	0.189
4	422.57	369.64	402.39	0.540	0.688	0.184	430.02	369.74	409.32	0.825	0.975	0.187
5	419.94	369.35	400.11	0.491	0.639	0.183	425.99	369.45	405.72	0.724	0.873	0.186
6	417.46	369.06	397.97	0.449	0.597	0.182	422.44	369.16	402.58	0.642	0.791	0.184
7	415.10	368.78	395.94	0.411	0.559	0.181	419.26	368.87	399.78	0.574	0.723	0.183
8	412.84	368.49	394.01	0.378	0.526	0.180	416.36	368.59	397.24	0.516	0.665	0.181

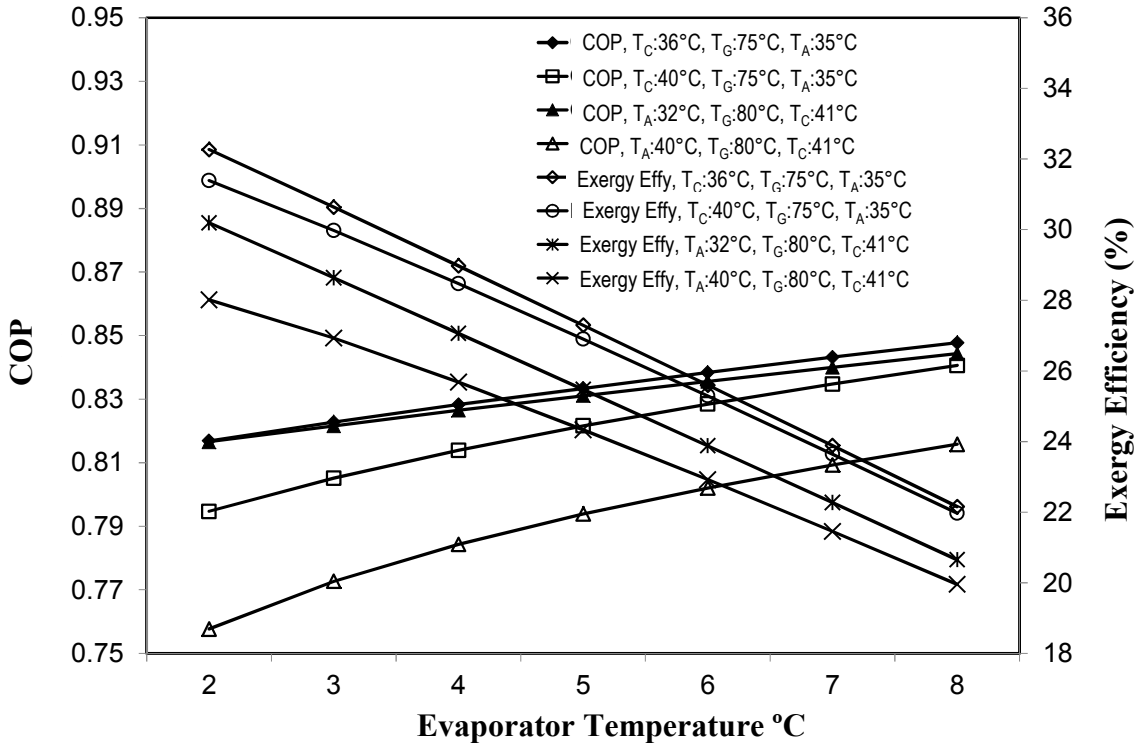

Fig. 3.2: Variation of COP and exergy efficiency with T_E at two different condenser and absorber temperatures

Variation of COP and exergy efficiency with T_E at two different absorber temperatures (T_A=32°C and T_A=40°C) is also shown in Fig. 3.2. In this case, T_G=80°C and T_C =41°C. Fig. 3.2 shows that COP and exergy efficiency decrease when T_A is increased at a given T_E . With increase in T_A the heat loads in the generator and absorber increase and it also causes increase in the mass flow rates. This is evident from the results in Table 3.6. The SP power increases due to increase in mass flow rate of the weak solution and as a result, the COP decreases because the evaporator cooling load is fixed (350 kW). Grover et al. [1] also reported higher COP at lower absorber temperature while showing COP variation with T_E at T_A=30°C and T_A=40°C keeping T_G and T_C fixed at 80°C and 40°C respectively.

Variation of total system irreversibility with T_E at two different condenser temperatures (T_C =36°C and T_C =40°C) and two absorber temperatures (T_A=32°C and T_A =40°C) is shown in Fig. 3.3 (a–b).

Table 3.6: Variation of component heat loads and mass flow rates with T_E at two different absorber temperatures

T_E (°C)	At T_G=80°C, T_C=41°C and T_A=32°C						At T_G=80°C, T_C=41°C and T_A=40°C					
	Heat Load (kW)			Mass Flow Rate (kg/s)			Heat Load (kW)			Mass Flow Rate (kg/s)		
	$\dot{Q}_G$	$\dot{Q}_C$	$\dot{Q}_A$	$\dot{m}_{ws}$	$\dot{m}_{ss}$	$\dot{m}_s$	$\dot{Q}_G$	$\dot{Q}_C$	$\dot{Q}_A$	$\dot{m}_{ws}$	$\dot{m}_{ss}$	$\dot{m}_s$
2	428.61	371.77	406.19	0.468	0.618	0.188	461.93	371.77	438.23	1.698	1.848	0.202
3	425.98	371.48	403.93	0.429	0.578	0.187	452.97	371.48	429.95	1.382	1.532	0.199
4	423.49	371.19	401.79	0.394	0.544	0.186	446.23	371.19	423.78	1.159	1.309	0.196
5	421.11	370.90	399.76	0.364	0.513	0.185	440.85	370.90	418.89	0.992	1.142	0.193
6	418.84	370.61	397.82	0.336	0.486	0.184	436.36	370.61	414.85	0.863	1.012	0.191
7	416.65	370.32	395.97	0.312	0.461	0.183	432.47	370.32	411.39	0.760	0.909	0.190
8	414.54	370.03	394.18	0.289	0.439	0.182	429.03	370.03	408.34	0.676	0.825	0.188

It is seen that the total system irreversibility increases with increase in T_E, but actually an opposite trend was expected as the COP was more at higher T_E. It was observed that the total irreversibility increases at higher T_E mainly due to increase in irreversibility of the generator and absorber.

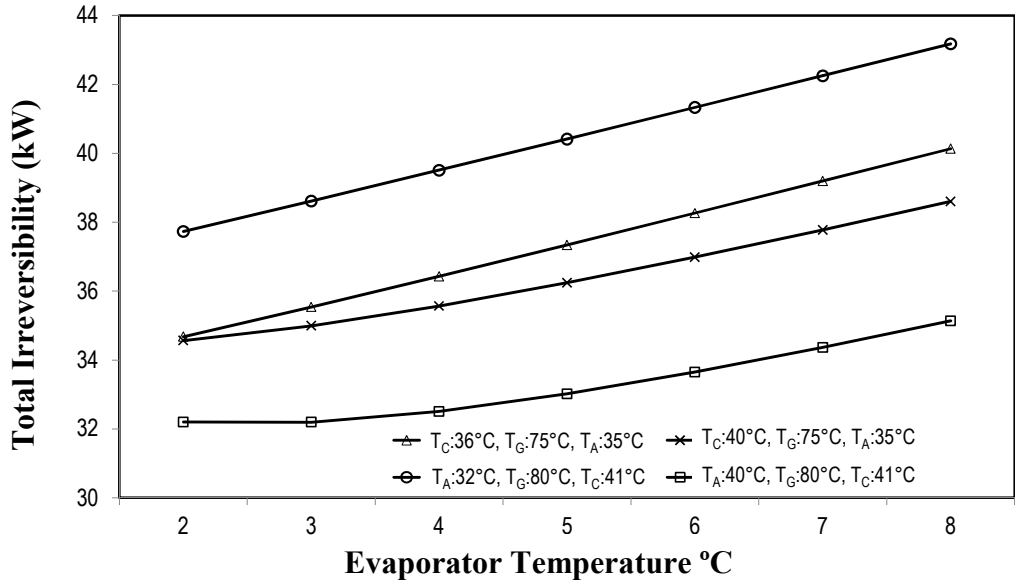

Fig. 3.3: Variation of total irreversibility with T_E at two different condenser and absorber temperatures

When T_E is increased, the specific exergy at state point 7 (ψ_7) decreases (from 76.779 kJ/kg at T_E =2°C to 43.406 kJ/kg at T_E =8°C when T_G=80°C T_C =41°C and T_A =40°C) while the specific exergy at the other state points (1, 8, 13 and 14) doesn't change. Also the mass flow rates ($\dot{m}_{ws}$, $\dot{m}_{ss}$, $\dot{m}_r$ and $\dot{m}_s$) decrease with T_E, therefore the difference in magnitude of the positive and negative terms increases in Equation 3.8 and this causes an increase in the generator irreversibility ($\dot{I}_G$). Similar increase in T_E (other temperatures fixed) also causes decrease in ψ_4 and ψ_5. Although the specific exergy at state points 10 to 12 don't change with T_E but with reduction in mass flow rates, finally the absorber also produces more irreversibility at higher T_E. In the other components (condenser, evaporator, SHE and expansion valve) irreversibility decreases with T_E, however magnitude wise the increase in the generator and absorber irreversibility is more compared to irreversibility decrease in the other components. Again since the COP and the exergy efficiency were more at T_C =36°C, therefore the total irreversibility

should have been less at T_C=36°C compared to its value at T_C=40°C, but a reverse trend is observed. Irreversibility is also more at T_A=32°C compared to its value at T_A=40°C at all evaporator temperatures although the COP and the exergy efficiency were higher at lower T_A.

While trying to analyze this contradiction it was found that it happens because of the water temperatures at entry and exit of the condenser, evaporator and absorber which are considered to vary with T_C, T_E and T_A as shown in Table 3.1. Instead of variable water temperatures, if fixed water temperatures are considered say e.g. 25°C at inlet and 30°C at outlet of the condenser and the absorber; 25°C at evaporator inlet and 10°C at evaporator outlet, then the COP values remain unchanged and show the same increasing trend with T_E while the exergy efficiency now increases and total system irreversibility decreases with T_E. Besides this, the total system irreversibility at a given T_E now becomes less at T_C=36°C compared to its value at T_C=40°C. However, the exergy efficiency which was earlier 32.271% at T_E=2°C and T_C=36°C with variable water temperatures now reduces to 12.693% if fixed water temperatures are considered. Similarly, the total system irreversibility also increases from 34.675 kW to 56.219 kW with this change in variable to fixed water temperatures. Variable water temperatures at inlet and exit of the VARS components are assumed because similar water temperatures were considered in Ref. [13] and now it is found that the VARS exergetic performance is greatly improved with variable water temperatures.

3.5.4 Performance variation with T_G at two different condenser and absorber temperatures

Fig. 3.4 (a–b) shows the variation of COP and exergy efficiency with T_G at two different condenser temperatures (T_C=38°C and T_C=46°C). T_A and T_E are kept fixed at 32°C and 8°C respectively. When T_C=38°C, T_G is varied from 68°C to 77°C while at T_C =46°C, range of T_G is taken from 76°C to 85°C. The different range of T_G is selected for the two condenser temperatures in order to keep the weak solution concentration within 50% limit. Results show that COP decreases continuously with increase in T_G at T_C =38°C while at T_C=46°C, initially it shows a slight increasing trend and maximum COP

(0.838) is obtained at T_G=77°C which then again decreases slightly with increase in T_G. COP is more at T_C=38°C compared to its value at T_C=46°C over the entire range of T_G. COP mainly decreases due to increase in Q_G value at higher T_G at both the condenser temperatures.

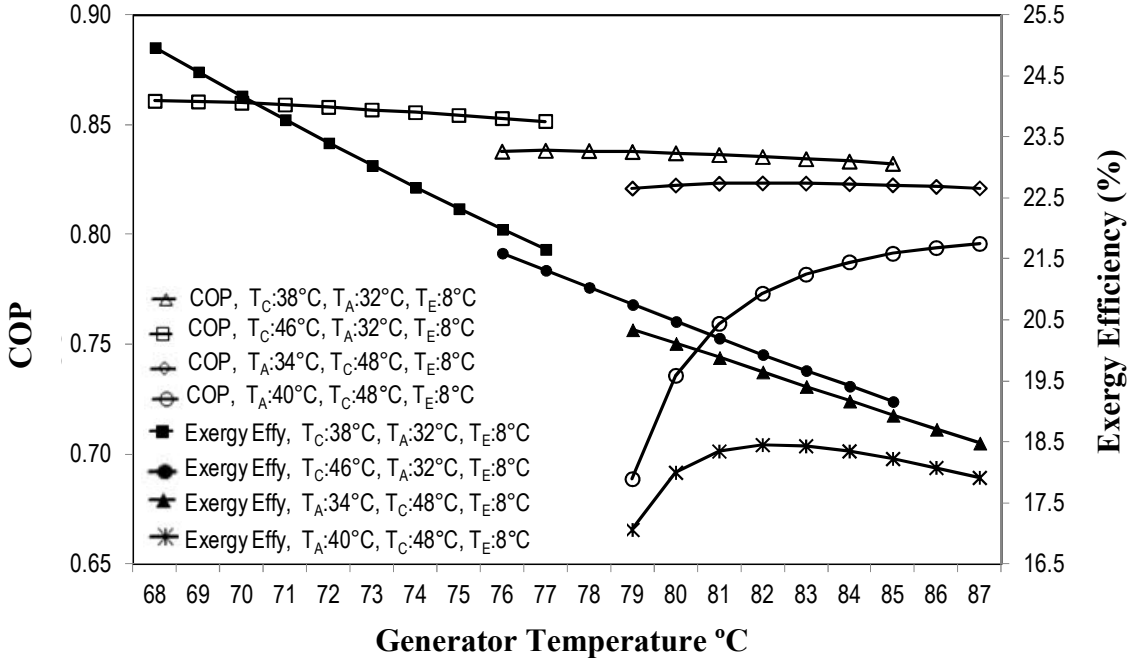

Fig. 3.4: Variation of COP and exergy efficiency with T_G at two different condenser and absorber temperatures

Table 3.7 shows the variation of component heat loads and mass flow rates with T_G at the two condenser temperatures. The SP power reduces at higher T_G due to reduction in weak solution mass flow rate ($\dot{m}_{ws}$) but usually the SP power value is negligible compared to Q_G, hence reduction in SP power does not affect COP much. Exergy efficiency also reduces with increase in T_G at both the condenser temperatures and compared to exergy efficiency value at T_C=46°C, its value is more at T_C=38°C.

Variation of COP and exergy efficiency with T_G at two different absorber temperatures (T_A=34°C and T_A=40°C) is also shown in Fig. 3.4 (a–b). In this case, T_C and T_E are kept fixed at 48°C and 8°C respectively and T_G is varied from 79°C to 87°C. COP more or less remains constant with T_G when T_A is 34°C whereas at T_A=40°C it

shows that COP increases from 0.689 at T_G=79°C to 0.796 at T_G=87°C. This is directly related with enthalpy variation in various state points leading to variation in component heat loads and mass flow rates. Results in Table 3.8 show that when T_A is 34°C, the generator heat '$\dot{Q}_G$' does not change much with T_G however the SP power shows a decreasing trend. Since $\dot{Q}_G$ is almost the same at various generator temperatures at T_A =34°C and as it is dominant over SP power, therefore COP does not vary much with T_G. On the other hand at T_A=40°C, $\dot{Q}_G$ decreases continuously from 508.29 kW at T_G=79°C to 439.83 kW at T_G=87°C. Similarly the SP power also decreases causing an overall increase in COP at higher T_G. Grover et al. [1] also observed similar COP variation with T_G at T_A=40°C. The exergy efficiency at T_A=34°C shows that it decreases linearly with T_G while the same in case of T_A=40°C first increases, reaches a maximum value of 18.448% at T_G=82°C and then again decreases with further increase in T_G. Further it is seen that COP and exergy efficiency are more at T_A=34°C compared to their values at 40°C over the entire range of T_G.

Table 3.7: Variation of component heat loads and mass flow rates with T_G at two different condenser temperatures

T_G (°C)	At T_E =8°C, T_A=32°C and T_C =38°C						At T_E =8°C, T_A=32°C and T_C =46°C					
	Heat Load (kW)			Mass Flow Rate (kg/s)			Heat Load (kW)			Mass Flow Rate (kg/s)		
	$\dot{Q}_G$	$\dot{Q}_C$	$\dot{Q}_A$	$\dot{m}_{ws}$	$\dot{m}_{ss}$	$\dot{m}_s$	$\dot{Q}_G$	$\dot{Q}_C$	$\dot{Q}_A$	$\dot{m}_{ws}$	$\dot{m}_{ss}$	$\dot{m}_s$
68	406.60	366.57	389.56	0.558	0.707	0.176	-	-	-	-	-	-
69	406.72	366.85	389.43	0.505	0.654	0.176	-	-	-	-	-	-
70	407.01	367.13	389.46	0.462	0.610	0.176	-	-	-	-	-	-
71	407.42	367.41	389.60	0.425	0.573	0.177	-	-	-	-	-	-
72	407.92	367.70	389.84	0.393	0.542	0.177	-	-	-	-	-	-
73	408.48	367.98	390.13	0.366	0.515	0.178	-	-	-	-	-	-
74	409.08	368.26	390.47	0.343	0.491	0.178	-	-	-	-	-	-
75	409.70	368.54	390.83	0.322	0.471	0.179	-	-	-	-	-	-
76	410.34	368.82	391.20	0.304	0.452	0.179	417.74	369.00	398.10	0.568	0.718	0.182
77	410.98	369.10	391.59	0.287	0.436	0.179	417.57	369.29	397.67	0.515	0.666	0.182
78	-	-	-	-	-	-	417.60	369.58	397.45	0.471	0.622	0.183
79	-	-	-	-	-	-	417.80	369.86	397.39	0.434	0.585	0.183
80	-	-	-	-	-	-	418.11	370.15	397.44	0.402	0.553	0.183
81	-	-	-	-	-	-	418.51	370.44	397.57	0.375	0.526	0.184
82	-	-	-	-	-	-	418.96	370.73	397.77	0.351	0.502	0.184
83	-	-	-	-	-	-	419.47	371.01	398.01	0.330	0.481	0.184
84	-	-	-	-	-	-	419.99	371.30	398.28	0.312	0.462	0.185
85	-	-	-	-	-	-	420.54	371.59	398.56	0.295	0.446	0.185

Table 3.8: Variation of component heat loads and mass flow rates with T_G at two different absorber temperatures

T_G (°C)	At T_E =8°C, T_C =48°C and T_A =34°C						At T_E =8°C, T_C =48°C and T_A =40°C					
	Heat Load (kW)			Mass Flow Rate (kg/s)			Heat Load (kW)			Mass Flow Rate (kg/s)		
	$\dot{Q}_G$	$\dot{Q}_C$	$\dot{Q}_A$	$\dot{m}_{ws}$	$\dot{m}_{ss}$	$\dot{m}_s$	$\dot{Q}_G$	$\dot{Q}_C$	$\dot{Q}_A$	$\dot{m}_{ws}$	$\dot{m}_{ss}$	$\dot{m}_s$
79	426.29	369.91	405.53	0.696	0.847	0.187	508.29	369.91	484.15	3.808	3.959	0.222
80	425.56	370.20	404.58	0.623	0.774	0.186	475.74	370.20	452.72	2.456	2.607	0.208
81	425.18	370.49	403.96	0.563	0.714	0.187	460.89	370.49	438.25	1.813	1.964	0.202
82	425.05	370.77	403.59	0.514	0.665	0.187	452.70	370.77	430.16	1.437	1.588	0.199
83	425.10	371.06	403.39	0.473	0.624	0.187	447.70	371.06	425.15	1.190	1.341	0.197
84	425.28	371.35	403.32	0.438	0.589	0.187	444.47	371.35	421.83	1.015	1.166	0.196
85	425.55	371.64	403.34	0.408	0.559	0.188	442.31	371.64	419.53	0.885	1.036	0.195
86	425.88	371.93	403.42	0.381	0.533	0.188	440.84	371.93	417.90	0.785	0.936	0.195
87	426.27	372.22	403.56	0.358	0.510	0.188	439.83	372.22	416.71	0.705	0.856	0.194

Fig. 3.5 shows that total system irreversibility increases linearly with T_G at both the condenser temperatures. When T_G is increased keeping the other component temperatures fixed, the total system irreversibility increases due to irreversibility increase in the generator, condenser and the absorber at higher T_G. Irreversibility in the evaporator and the expansion valve 1 is not affected by change in T_G and it is only the SHE where irreversibility shows reduction at higher T_G. Again the total system irreversibility at a fixed generator temperature is more at T_C=38°C compared to its value at T_C=46°C. At T_G=77°C, the total irreversibility values are 43.254 kW and 35.224 kW at T_C=38°C and 46°C respectively. This happens mainly due to the VARS generator and absorber irreversibility which reduce by 4.516 kW and 4.457 kW when T_C is changed from 38°C and 46°C. Condenser irreversibility also reduces slightly by 0.486 kW. Irreversibility in the evaporator does not change while the irreversibility in the SHE and expansion valve 1 increases by 0.839 kW and 0.591 kW respectively due to increase in T_C from 38°C and 46°C at T_G=77°C. At higher T_C, the heat loads in the VARS components, particularly in the generator and absorber are more (Table 3.7). The mass flow rates ($\dot{m}_{ws}$, $\dot{m}_{ss}$ and $\dot{m}_s$) also increase with T_C. Moreover with increase in T_C from 38°C and 46°C at T_G=77°C, the specific exergy at state point 1 (ψ_1) increases from 108.984 kJ/kg to 166.657 kJ/kg and while at the state point 7, the specific exergy increases from 2.837 kJ/kg to 4.001 kJ/kg.

On the other hand, the specific exergy at state point 8 (ψ_8) decreases from 111.277 kJ/kg at T_C=38°C to 58.503 kJ/kg at T_C=46°C. Decrease in ψ_8 doesn't cause much change because $\dot{m}_{ws}$ also increases simultaneously at T_C =46°C. The main difference in generator irreversibility at T_C=38°C and T_C=46°C (less at higher T_C) arises due to increase in $\dot{m}_r$ and ψ_1 as the term $\dot{m}_r\psi_1$ is subtracted in Equation 3.8 that is used for calculation of $\dot{I}_G$. Specific exergy at the state points 1, 7 and 8 also changes due to change in enthalpy and entropy at these points caused by the increase in generator pressure (equal to condenser pressure) from 6.632 kPa to 10.01 kPa and reduction in weak solution concentration from 49.92% at T_C=38°C to 42.54% at T_C=46°C. The

absorber irreversibility also reduces at T_C =46°C mainly due to reduction in specific exergy at state point 10 (ψ_{10}) from 103.077 kJ/kg at T_C =38°C to 49.634 kJ/kg at T_C =38°C.

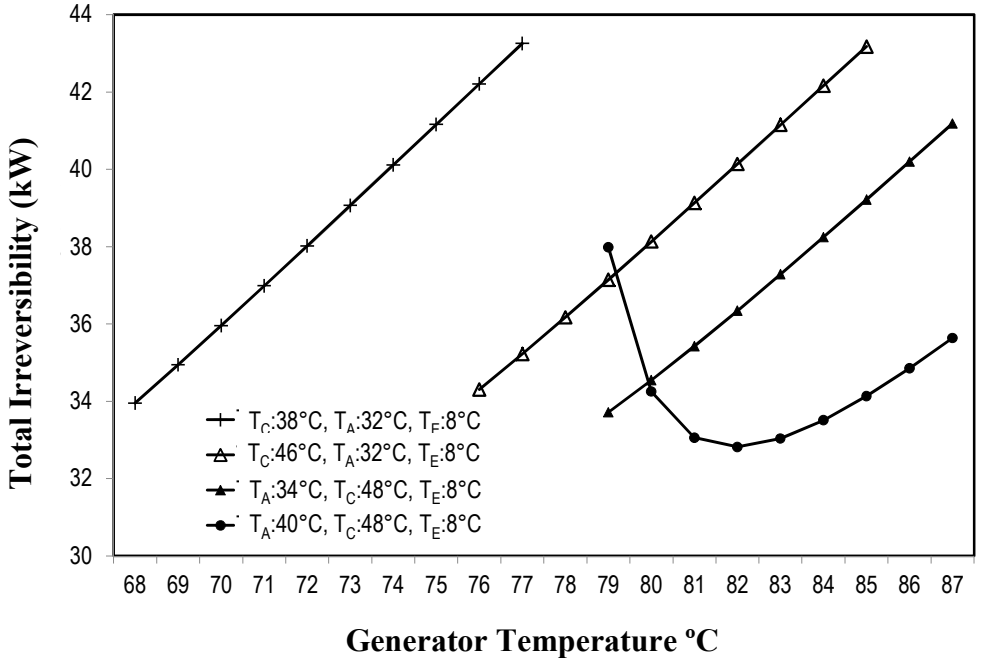

Fig. 3.5: Variation of total irreversibility with T_G at two different condenser and absorber temperatures

The exergy at the other state points in Equation 3.9 (used for calculation of $\dot{I}_A$) is not affected due to change in T_C from 38°C and 46°C at T_G =77°C. However since COP was more at T_C =38°C, therefore a lesser value of irreversibility was expected at T_C =38°C. This is however not the case and irreversibility is more at T_C =38°C due to variable water temperatures considered in this Chapter. Instead of variable temperatures if the same fixed water temperatures as mentioned in Section 3.5.3 are considered, then irreversibility becomes less at T_C =38°C (55.535 kW) compared to its value at T_C =46°C (56.417 kW) at T_G =77°C, T_A =32°C and T_E =8°C. However with fixed water temperatures, the system produces more irreversibility (55.535 kW at T_C =38°C against 43.254 kW with variable water temperatures) and exergy efficiency becomes significantly low (12.877% with fixed and 21.66% with variable water temperatures).

The total system irreversibility variation with T_G at the two absorber temperatures (T_A=34°C and T_A=40°C) is also shown in Fig. 3.5. At T_A=34°C, total system irreversibility increases linearly with T_G while at T_A=40°C, the irreversibility initially decreases and then again increases with the minimum irreversibility occurring at T_G=82°C. Further it is seen that the total system irreversibility is more at T_A=34°C (but actually a lower value is desired as the COP and exergy efficiency are higher at T_A =34°C) than its value at T_A=40°C over the selected range of T_G except at T_G=79°C. It was observed that $\dot{I}_G$ which contributes maximum to the total system irreversibility was less at T_A=40°C at various generator temperatures and the difference in $\dot{I}_G$ value at T_A =34°C and T_A=40°C was the minimum at T_G=79°C. Irreversibility in the condenser, evaporator and the expansion valve 1 at a given T_G does not change much with T_A although the values are different at different T_G . The main reason of lower total irreversibility only at T_G =79°C corresponding to T_A =34°C was due to SHE irreversibility which is less at T_A=34°C compared to its value at T_A=40°C. At the other generator temperatures also, SHE irreversibility corresponding to T_A=34°C is less but the difference between $\dot{I}_{SHE}$ value at T_A =40°C and T_A =34°C gradually decreases with increase in T_G. Hence, due to $\dot{I}_G$ which is always higher at T_A=34°C and $\dot{I}_{SHE}$ difference being gradually low, finally the total irreversibility becomes more at T_A=34°C from T_G =80°C and beyond. This is however the case with variable water temperatures (Table 3.1). At fixed water temperatures too, irreversibility variation with T_G follow the same pattern, but the system irreversibility at T_A=34°C is less than its value at T_A=40°C over the entire T_G range from 79°C to 87°C. Further the total system irreversibility which was earlier less with variable water temperatures now becomes higher and exergy efficiency also reduces significantly when fixed water temperatures are considered.

3.5.5 Performance comparison between H_2O–LiCl and H_2O–LiBr VARS

The energetic performance between H_2O–LiCl and H_2O–LiBr VARS was compared in an identical condition by Grover et al. [1] in terms of COP considering a reference state of zero enthalpy at 6.89% concentration and 0°C temperature for both

H_2O–LiCl and H_2O–LiBr solutions. She at al. [4] also made performance comparison of a single stage VARS using H_2O–LiCl and H_2O–LiBr solution pairs and evaluated COP at same operating conditions of the two systems (T_E =5°C, T_C = T_A =35°C, 15°C temperature difference in the SHE and 10°C temperature difference between heat source and generator). In the present study also, performance comparison between the two systems are provided but not only in terms of COP, also in terms of their exegetic performance parameters. For simulating the performance of the H_2O–LiBr VARS, correlations of Lansing [14] are used to determine the temperature dependent weak and strong solution concentration of the H_2O–LiBr solution. Thermodynamic properties (specific heat, density, enthalpy and entropy) of H_2O–LiBr solutions at various temperatures and concentrations are calculated using the correlations of Patek and Klomfar [16]. Same operating temperatures of the two systems are considered and the results are compared in Table 3.9 for seven such combinational temperatures. Results shows that COP and exergy efficiency of the H_2O–LiCl VARS are higher than those of the H_2O–LiBr system at all the temperature combinations considered. Grover et al. [1] also reported higher COP with H_2O–LiCl VARS which they attributed to lower FR of the H_2O–LiCl system. Similarly, She at al. [4] also, while varying the heat source (hot water) temperature from 80°C to 100°C, found that the COP of the H_2O–LiCl VARS was higher over the entire range of heat source temperatures and particularly in the lower heat source temperature, the COP difference between the two systems was more prominent. In this study, it is seen that not only the COP but the exergy efficiency is also more and the total irreversibility reduces when the system is operated with H_2O–LiCl solution. The generator is the most crucial among the VARS components that contributes maximum to the total irreversibility in both the systems. This is depicted in Fig. 3.6 which shows the irreversibility distribution in various system components of the two systems at T_E =5°C, T_G =66C, T_C =28°C and T_A =35°C.

Table 3.9: Performance comparison of the $H_2O-LiCl$ and $H_2O-LiBr$ VARS at some selected component temperatures

Temperature (°C)				$H_2O-LiCl$ VARS					$H_2O-LiBr$ VARS				
T_E	T_G	T_C	T_A	COP	X_{ws}	X_{ss}	$\dot{I}_{tot}$ (kW)	η (%)	COP	X_{ws}	X_{ss}	$\dot{I}_{tot}$ (kW)	η (%)
4	70	31	31	0.855	0.498	0.351	40.775	32.169	0.794	0.578	0.536	45.536	29.887
4	69	31	35	0.842	0.489	0.392	35.500	32.181	0.697	0.573	0.559	47.244	26.670
5	66	28	35	0.856	0.488	0.383	36.600	32.133	0.769	0.575	0.552	42.538	28.886
6	72	33	37	0.839	0.499	0.395	36.286	26.741	0.730	0.576	0.557	44.836	23.262
8	63	25	37	0.872	0.486	0.379	37.707	27.532	0.819	0.578	0.543	40.698	25.862
8	85	46	39	0.807	0.497	0.399	36.309	18.573	0.585	0.565	0.555	62.609	13.479
9	66	28	34	0.877	0.488	0.341	41.660	24.104	0.837	0.575	0.520	44.204	23.001

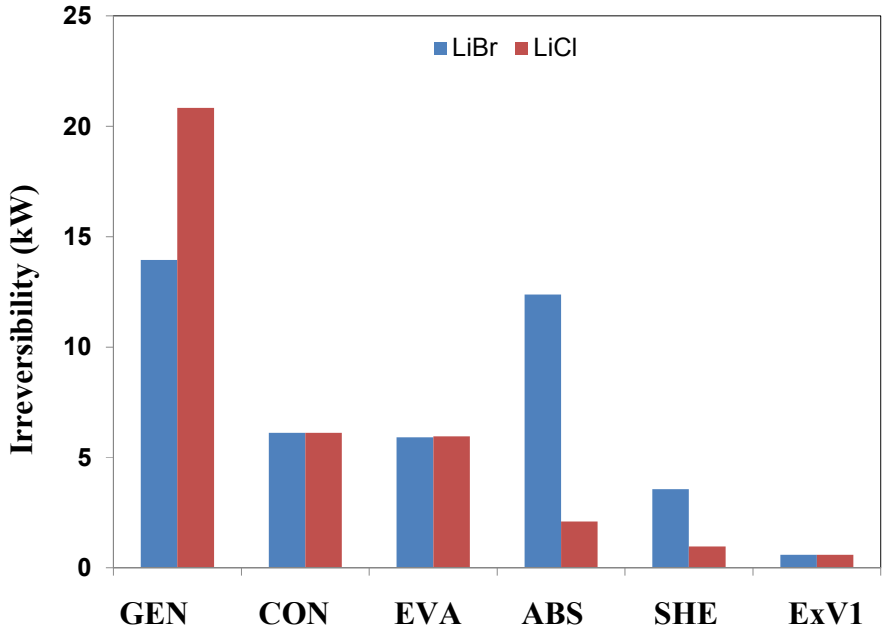

Fig. 3.6: Irreversibility of different components of H_2O−LiCl and H_2O−LiBrVARS at T_E =5°C, T_G=66°C, T_C=28°C and T_A=35°C

The generator irreversibility of the H_2O–LiCl VARS is however more compared to that of the H_2O–LiBr system. The specific exergies of steam entering and leaving the generator (ψ_{13} and ψ_{14}) are the same (same T_G) in both the systems, but $\dot{m}_s$ is different because $\dot{Q}_G$ is not the same in the two systems. Due to enthalpy of working pair solutions being different at state points 7 and 8, $\dot{Q}_G$ becomes less in the H_2O–LiCl system which is 409.116 kW against a $\dot{Q}_G$ value of 455.05 kW corresponding to the H_2O–LiBr system. Hence, the generator steam flow rate requirement ($\dot{m}_s$) in the H_2O–LiCl system reduces which is 0.177 kg/s against 0.196 kg/s of the H_2O–LiBr system. Due to this reason, the steam side net efflux of exergy becomes less in the H_2O–LiCl system generator (59.760 kW against 66.470 kW of the H_2O–LiBr VARS generator). However, the negative difference between strong solution exergy at state point 7 ($\dot{m}_{ss}\psi_7$) and weak solution exergy at state point 8 ($\dot{m}_{ws}\psi_8$) is less and therefore the generator irreversibility is more in the H_2O–LiCl system. Irreversibility in the condenser, evaporator and expansion valve 1 of the two systems are more or less the same. The difference in the total irreversibility of the two systems mainly arises due to the absorber and the SHE irreversibility, particularly in the absorber; the irreversibility is significantly less in the H_2O–LiCl system. Refrigerant mass flow rate ($\dot{m}_r$) and specific exergy at

state point 4 (ψ_4) are the same in both the systems (same evaporator cooling load) which are 0.146 kg/s and -176.129 kJ/kg respectively, however $\dot{m}_{ws}$ and $\dot{m}_{ss}$ are different. Weak solution mass flow rate, $\dot{m}_{ws}$ which is 3.492 kg/s in the H_2O–LiBr system reduces to 0.537 kg/s in the H_2O–LiCl system. Similarly $\dot{m}_{ss}$ is also less in H_2O–LiCl system; it is 0.684 kg/s compared to 3.638 kg/s of the H_2O–LiBr system. As a result, the FR in the H_2O–LiCl VARS reduces significantly. FR value in H_2O–LiCl system is 3.672 compared to 23.869 of the H_2O–LiBr system. Specific exergy at the state points 5 and 10 of the two systems are also different. In the H_2O–LiCl VARS, ψ_5 =24.498 kJ/kg and ψ_{10} =93.889 kJ/kg whereas these values are 26.509 kJ/kg and 40.422 kJ/kg in the H_2O–LiBr system. Changes in the values of ψ_5 and ψ_{10} also cause difference in absorber irreversibility of the two systems. For similar reasons, the SHE irreversibility is also less in the H_2O–LiCl system. Thus it was observed that although the refrigerant mass rate remains the same but the mass flow rates of the weak solution at absorber outlet and the medium solution at absorber inlet are different in the two systems. The solution mass flow rates are more in the double effect systems when they are operated with H_2O–LiBr. Moreover the properties of the two salt solutions are also different. The combined effect of change in mass flow rates and properties finally affect the exergy at the state points 5 and 10 of the two systems. As a result, the absorber irreversibility in the double effect H_2O–LiBr systems becomes more compared to that of the H_2O–LiCl systems.

Additionally, to provide a clear cut understanding of exergy flow, the exergy flow diagrams of the single effect H_2O–LiCl and H_2O–LiBr VARS configurations are shown in Fig. 3.7 and Fig. 3.8 at T_G =66ºC, T_C =28ºC, T_A =34ºC and T_E =9ºC. It is observed that although the exergy input is different (slightly less with H_2O–LiCl) but the exergy output is the same in both the systems. The exergy losses in the evaporator of the two systems are also more or less same. The exergy loss in the generator of the H_2O–LiCl based system is however more compared to that of the H_2O–LiBr counterpart. The main difference arises due to the exergy loss in the absorber which in the single effect H_2O–LiCl system (8 %) is less compared to that of the H_2O–LiBr (22.77 %). The other unaccounted exergy loss which is about 4.43 % in the H_2O–LiCl system is also relatively less comared to 4.64 % of the H_2O–LiBr. Similar results corresponding to components'

exergy losses were also depicted in Fig. 3.6 which were shown for T_G=66ºC, T_C=28ºC, T_A=35 ºC and T_E=5ºC.

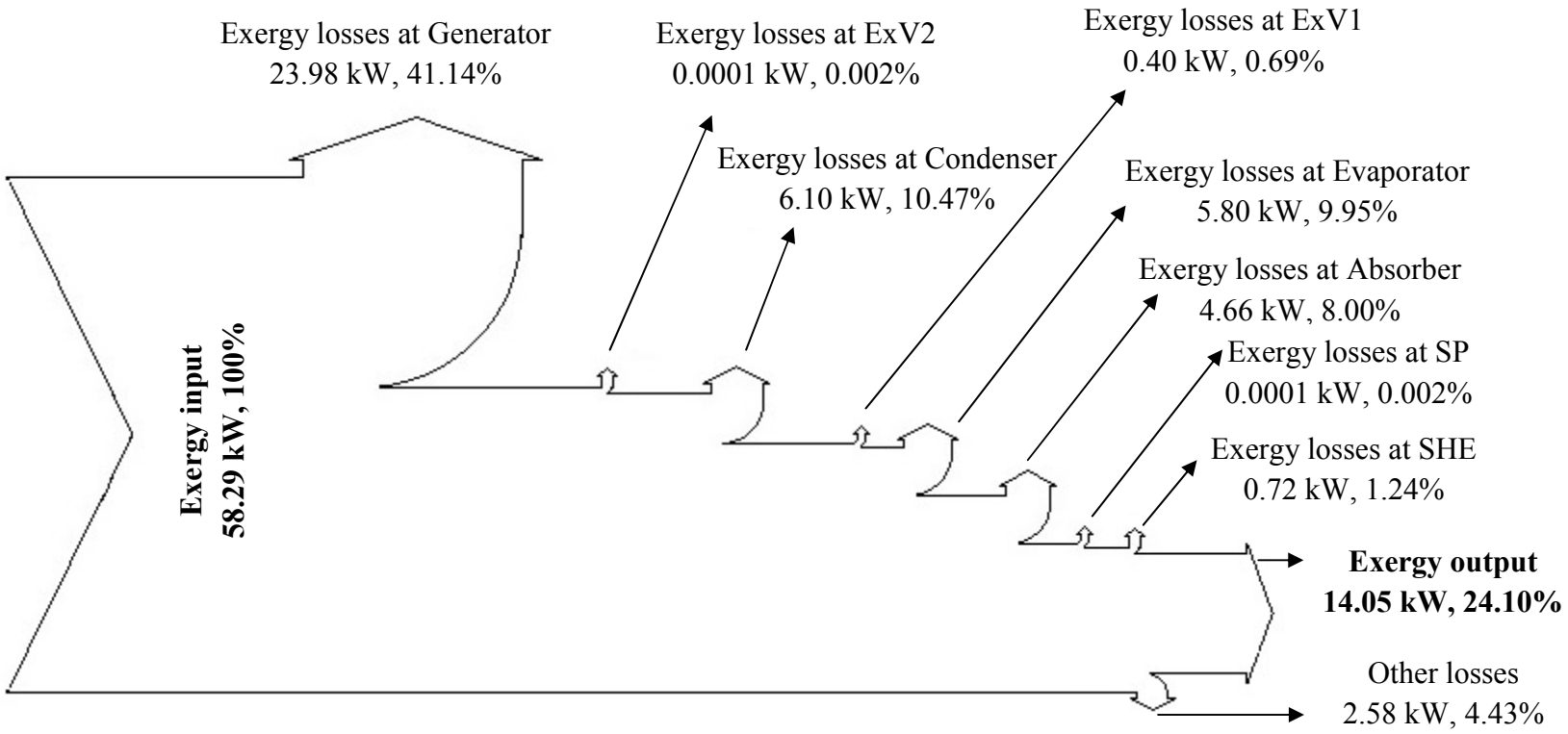

Fig. 3.7: Exergy flow diagram of the single effect H_2O–LiCl system at T_G=66ºC, T_C=28ºC, T_A=34ºC and T_E=9ºC

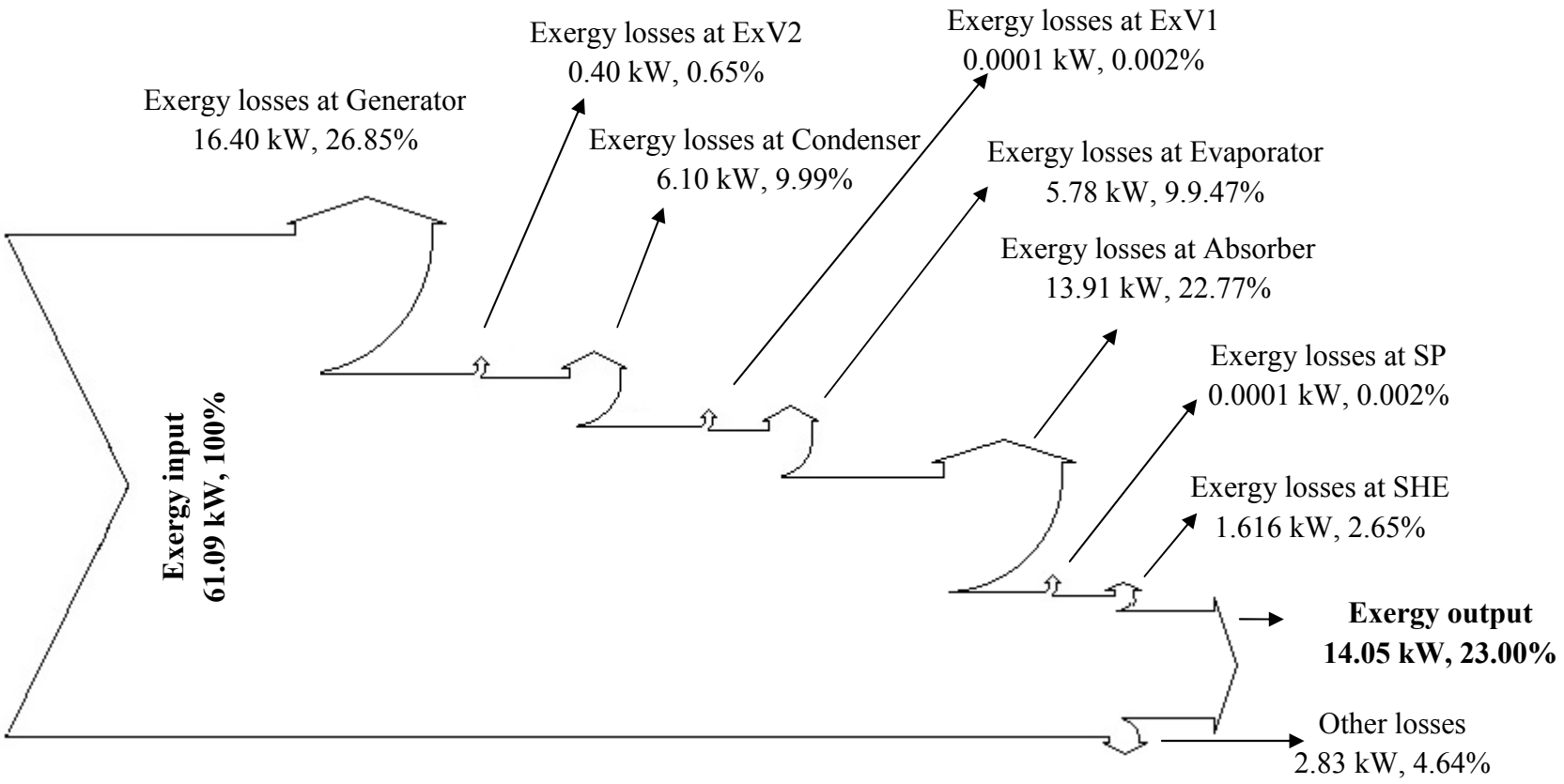

Fig. 3.8: Exergy flow diagram of the single effect H_2O–LiBr system at T_G=66ºC, T_C=28ºC, T_A=34ºC and T_E=9ºC

3.6 Summary

In this Chapter, the operating temperatures of a H_2O–LiCl VARS are estimated using an inverse technique considering weak solution concentration ($X_{ws} \leq 50\%$) as objective function and a DE based optimization method. Total 34 different combinations of temperatures are obtained within the prescribed range of lower and upper bound of the component temperatures. It was observed from the estimated temperatures that when a lower T_G is estimated by the inverse method, the corresponding estimated T_C also reduces proportionately and the vice versa. This was due to direct dependence of X_{ws} on T_G and T_C as defined in the problem.

Next the energetic and exergetic performance of the H_2O–LiCl VARS is evaluated with the estimated temperature combinations at a fixed evaporator cooling load of 350 kW. Further, a parametric analysis is performed separately to show performance variation with component temperatures. Parametric variation showed that the COP of the H_2O–LiCl VARS improves when evaporator temperature is increased keeping the other component temperatures fixed. COP is also more at lower values of T_G, T_C and T_A. It was expected that when COP increases, exergy efficiency should also increase and total system irreversibility should decrease. However in case of the exergy efficiency and the total system irreversibility, an opposite trend was observed. This contradiction mainly aroused due to the water temperatures at inlet and outlet of the respective VARS components which was assumed to vary with the component temperatures in this study. An increasing trend of exergy efficiency similar to that of COP and also with simultaneously decreasing total irreversibility can be obtained if fixed water temperatures are considered instead of variable, however in that case the exergy efficiency value becomes less and the magnitude of total irreversibility increases due to higher temperature difference between the two mediums.

Specifically, from the results corresponding to T_G variation it was found that there is an upper limit of T_G. The limit up to which T_G can be increased is actually fixed by the condenser temperature and beyond the limit, X_{ws} exceeds 50%. Higher the value of T_C, upper is the limit of T_G. E.g. when T_C =38°C, T_G can be increased maximum up to 77°C, and again when T_C is 46°C, the maximum possible upper limit of T_G is 85°C. Thus in

general a 39°C temperature difference between T_G and T_C was noticed which was also evident in various combinations of temperatures estimated from inverse analysis. Further it was seen that the trend of variation of COP, exergy efficiency and total irreversibility with T_G is specific to the chosen values of the other component temperatures (T_C, T_E and T_A).

From the performance comparison between the H_2O–LiCl and H_2O–LiBr VARS, it was observed that the H_2O–LiCl system performs better than the H_2O–LiBr system under identical condition of operating temperatures. COP and exergy efficiency are higher while the total system irreversibility is less in the H_2O–LiCl VARS compared to those of the H_2O–LiBr system. This was mainly due to the thermodynamic properties of aqueous H_2O–LiCl solution and lower FR in case of the H_2O–LiCl VARS. Although the generator irreversibility was more in the H_2O–LiCl system, but the irreversibility values in the absorber and SHE were significantly less which finally contributed to lower total system irreversibility of the H_2O–LiCl VARS.

Bibliography

[1] Grover, G. S., Eisa, M. A. R., and Holland, F. A. Thermodynamic design data for absorption heat pump systems operating on water–Lithium Chloride–Part one. Cooling. *Heat Recovery Systems and CHP,* 8: 33−41, 1988.

[2] Won, S. H. and Lee, W. Y. Thermodynamic Design Data for Double–Effect Absorption Heat Pump Systems Using Water–Lithium Chloride Cooling. *Heat Recovery Systems and CHP,* 11:41−48, 1991.

[3] Saravanan, R. and Maiya, M. P. Thermodynamic comparison of water–based working fluid combinations for a vapor absorption refrigeration system. *Applied Thermal Engineering,* 18: 553–568, 1998.

[4] She. X., Yin, Y., Xu, M., and Zhang, X. A novel low–grade heat–driven absorption refrigeration system with LiCl–H_2O and LiBr–H_2O working pairs. *International Journal of Refrigeration,* 58: 219–34, 2015.

[5] Conde, M. R. Properties of aqueous solutions of Lithium and Calcium chlorides: formulations for use in air conditioning equipment design. *International Journal of Thermal Science,* 43:367–82, 2004.

[6] Patek, J. and Klomfar, J. Solid–liquid phase equilibrium in the systems of LiBr–H_2O and LiCl–H_2O. *Fluid Phase Equilibrium,* 250:138–49, 2006.

[7] Patek, J. and Klomfar, J. Thermodynamic properties of the LiCl–H_2O system at vapour–liquid equilibrium from 273 K to 400 K. *International Journal of Refrigeration,* 31:287–303, 2008.

[8] Ardia, D., Boudt, K., Carl, P., Mullen, K., and Peterson, B.G. Differential Evolution with DEoptim, An Application to Non–Convex Portfolio Optimization. *The Research Journal,* 3:27−34, 2011.

[9] Mallipeddi, R., Suganthan, P. N., Pan, Q. K., and Tasgetiren, M. F. Differential evolution algorithm with ensemble of parameters and mutation strategies. *Applied Soft Computing*, 11:1679–96, 2011.

[10] Gogoi, T. K., Pandey, M., and Das, R. Estimation of operating parameters of a reheat regenerative power cycle using simplex search and differential evolution based inverse methods. *Energy Conversion and Management,* 91:204–18, 2015.

[11] Gogoi, T. K. and Talukdar, K. Thermodynamic analysis of a combined reheat regenerative thermal power plant and water–LiBr vapour absorption refrigeration system. *Energy Conversion and Management,* 78:595–610, 2014.

[12] Gogoi, T. K. and Talukdar, K. Exergy based parametric analysis of a combined reheat regenerative thermal power plant and water–LiBr vapour absorption refrigeration system. *Energy Conversion and Management,* 83:119–32, 2014.

[13] Gomri, R. Second law comparison of single effect and double effect vapour absorption refrigeration systems. *Energy Conversion and Management,* 50: 1279–1287, 2009.

[14] Lansing, F. L. Computer modelling of a single stage Lithium Bromide/Water Absorption refrigeration unit. *JPL Deep Space Network Progress Report 42–32.* DSN Engineering section, 247–57, 1976.

[15] Wagner, W., Cooper, J. R., Dittmann, A., Kijima, J., Kretzschmar, H. J., Kruse, A., et al. The IAPWS Industrial Formulation 1997 for the thermodynamic properties of water and steam. *Journal of Engineering, Gas Turbine Power,* 122:150–81, 2000.

[16] Patek, J. and Klomfar, J. A computationally effective formulation of thermodynamic properties of LiBr–H_2O solutions from 273 to 500 K over full composition range. *International Journal of Refrigeration,* 29: 566–578, 2006.